EDGE ARTICLE

Check for updates

Double design of host and guest synergistically reinforces the Na-ion storage of sulfur cathodes†

Xiang Long Huang, [ID] *[a] Hong Zhong,[a] Ce Li,[a] Yaojie Lei,[c] Shaohui Zhang, [ID] [d] Yuhan Wu, [ID] [e] Wenli Zhang,[f] Hua Kun Liu,[bc] Shi Xue Dou [ID] *[bc] and Zhiming M. Wang*[ag]

Development of room-temperature sodium–sulfur batteries is significantly hampered by the shuttle effect of soluble intermediates and intrinsically sluggish conversion kinetics. In this work, a double design host and guest strategy (*i.e.*, implantation of a polar V_2O_3 adsorbent into a carbon substrate and selenium doping of a sulfur guest) is proposed to synergistically reinforce the electrochemical properties of sulfur electrodes in sodium ion storage. The V_2O_3 adsorbent efficiently immobilizes sulfur species *via* strong polar–polar interactions, while the selenium dopant improves the electronic conductivity of sulfur cathodes and accelerates the redox conversion of sulfur cathodes. The synergistic effect between the V_2O_3 adsorbent and selenium dopant is shown to inhibit the shuttle effect and improve the redox kinetics, thus realizing greatly enhanced Na-ion storage properties of sulfur cathodes. The as-designed sulfur cathode delivers a superior rate capability of 663 mA h g^{-1} at 2.0 A g^{-1} and demonstrates excellent cyclability of 405 mA h g^{-1} over 700 cycles at 1.0 A g^{-1}.

Introduction

Room-temperature sodium–sulfur (RT Na–S) batteries are deemed to be an emerging and promising electrochemical energy storage technology and have drawn extensive research interest over the past decade due to integrating the advantages of both elemental Na and S.[1,2] Their ubiquitous distribution in nature allows widespread and sustainable access to sodium resources and low-cost refinement of electrode materials. Moreover, the merits of high abundance, low cost, and non-toxicity make S an eco-friendly and large-scale commercial electrode material. Additionally, metallic Na and S demonstrate high theoretical specific capacities of 1166 and 1675 mA h g^{-1},

respectively.[3] Accordingly, RT Na–S batteries are cost-effective and high-energy density systems, which operate *via* a two-electron reaction pathway and show an impressive theoretical energy density of 1275 W h kg^{-1}.[4,5]

Although RT Na–S batteries can potentially meet all kinds of expectations for commercial applications, their development is hindered by challenges on the S cathode side. First, the low electronic conductivity of S and its discharge products leads to low utilization of active materials and large polarization.[6,7] Second, electrochemically-induced solvated polysulfide moieties often give rise to instability of the S cathode and corrosion of the Na anode.[8,9] Third, the dramatic volume variation of S cathodes is responsible for the microstructural deformation of materials and the pulverization of electrodes.[10] Another concerning issue is that RT Na–S chemistry has to contend with the sluggish redox kinetics of S speciation and the low solid-state diffusivity of Na ions.[11] These issues generally manifest in large voltage hysteresis in discharge–charge profiles, less well-defined and weak redox peaks in cyclic voltammetry (CV) curves, rapid capacity fading, and poor rate capabilities for RT Na–S batteries.

Engineering electrically conductive porous carbon hosts for dispersed encapsulation of S guest molecules has been widely shown to improve the electronic conductivity of S cathodes, confine the dissolution and shuttling of solvated polysulfides *via* the nanopore effect, and accommodate the volumetric fluctuation of active materials during the (de)sodiation process.[12,13] Nevertheless, the substantial nonpolar nature of carbons renders them with too poor chemical affinity for

[a]*Institute of Fundamental and Frontier Sciences, University of Electronic Science and Technology of China, Chengdu 611137, China. E-mail: xlhuang_uestc@163.com; zhmwang@uestc.edu.cn*

[b]*Institute of Energy Materials Science, University of Shanghai for Science and Technology, Shanghai 200093, China. E-mail: shi@usst.edu.cn*

[c]*Institute for Superconducting and Electronic Materials, University of Wollongong, NSW 2500, Australia. E-mail: shi@uow.edu.au*

[d]*Guangdong Provincial Key Laboratory of Micro/Nano Optomechatronic Engineering, College of Mechatronics and Control Engineering, Shenzhen University, Shenzhen 518060, China*

[e]*School of Environmental and Chemical Engineering, Shenyang University of Technology, Shenyang 110870, China*

[f]*School of Chemical Engineering and Light Industry, Guangdong University of Technology, 100 Waihuan Xi Road, Guangzhou 510006, China*

[g]*Institute for Advanced Study, Chengdu University, Chengdu 610106, China*

† Electronic supplementary information (ESI) available. See DOI: https://doi.org/10.1039/d2sc06831a

polysulfides to inhibit the shuttle effect thoroughly. A useful design strategy is to implant polar adsorbents (*e.g.*, heteroatoms and metal compounds) with strong bonding ability for polysulfides on/into conductive carbons, which can assist in capturing soluble polysulfides *via* surface polar sites to stabilize S cathodes.[14–17] In this context, how to improve the redox kinetics of S guest molecules needs to be urgently considered.

In recent years, the effect of eutectic accelerators (*i.e.*, Se doping for S) has been demonstrated as an effective strategy to regulate the electronic structure of S and boost the intrinsic kinetics of S cathodes, which exhibits some distinguished merits for redox conversions of S in comparison with the common design strategy of electrocatalysts.[18,19] First, Se dopant can be easily dispersed amongst S molecules *via* S–Se bonding at a molecular level to regulate the reactivity of S molecules. Second, despite a low doping content, the Se dopant is able to function as electrochemically active sites to contribute extra capacity *via* redox reactions with Na ions. Third, the Se dopant is proved to favor improved Na ion diffusion in kinetic processes, thus inducing faster redox kinetics.[20] Accordingly, such an approach has been attracting ever-increasing research interest, as the kinetic characteristics of S conversion can be regulated *via* the molecular design of guests instead of incorporating electrocatalysts into hosts.

In consideration of the significance of polar adsorption and Se doping for S conversion chemistry, we propose a double design host and guest strategy to inhibit the shuttle effect and improve the redox kinetics of RT Na–S batteries, that is, dispersing Se-doped S (SeS$_2$) into polar V$_2$O$_3$ decorated porous carbon (denoted as SeS$_2$/V$_2$O$_3$@C). Experimental and theoretical analysis shows that the V$_2$O$_3$ adsorbent is able to chemically capture sodium polysulfides/polyselenides *via* the formation of strong polar–polar interactions so as to stabilize the S cathode. The Se dopant induces higher capacity of the S electrode, due to its redox activity with Na ions, and more importantly, plays the role of accelerator in elevating the reaction kinetics of S cathodes. With the synergistic enhancement effect of host and guest, the as-designed SeS$_2$/V$_2$O$_3$@C cathode demonstrates good cyclability (405 mA h g^{-1} after 700 cycles at 1.0 A g^{-1}) and excellent rate capability (663 mA h g^{-1} at 2.0 A g^{-1}). This strategy opens up a new pathway for designing high-performance S cathodes for Na-ion storage and sheds light on the concept that the design of guest molecules is equally as important as that of host design.

Results and discussion

The design and fabrication process of the target material is schematically illustrated in Fig. 1a. The precursor was prepared as a template *via* a solvothermal method, the successful synthesis of which was confirmed from the X-ray diffraction (XRD) pattern and field-emission scanning electron microscopy (FESEM) image shown in Fig. S1 and S2,† in good accordance with the results of a previous study.[21] The precursor is thermally treated to form porous carbon nanorods under an insert atmosphere (Fig. S3 and S4†). Pure carbon exhibits too weak a chemical affinity for soluble polysulfides and polyselenides to

prevent their shuttle effect and hence, strong polar V$_2$O$_3$ nanoparticles are further grown onto the as-prepared carbon nanorods (V$_2$O$_3$@C), endowing them with improved capture ability for intermediates. Afterwards, the active SeS$_2$ is composited with the V$_2$O$_3$@C to produce the SeS$_2$/V$_2$O$_3$@C composite.

The V$_2$O$_3$@C nanocomposite inherits the nanorod-like shape, indicating that the growth process of V$_2$O$_3$ nanoparticles on porous carbon does not destroy the overall morphology and microstructure of the carbon substrate, as displayed in Fig. 1b. An interplanar spacing of 0.375 nm can be clearly witnessed from Fig. 2c, which actually corresponds to the (012) facet of V$_2$O$_3$ very well. In addition to that, it can be found that there is a tight coupling between polar V$_2$O$_3$ and the amorphous carbon structure, which is beneficial to the fast interfacial transport of electrons with improved kinetics. Internal nanocavities of the carbon nanorods can offer accommodation space for the inputted active materials, as clearly shown in Fig. 2d. The STEM image with corresponding EDS mappings in Fig. S5† reflect the uniform anchoring of V$_2$O$_3$ onto the carbon substrate. The content of V$_2$O$_3$ in the V$_2$O$_3$@C composite is about 26%, as shown in Fig. S6.† As SeS$_2$ is infused into the V$_2$O$_3$@C through a typical melt-diffusion method, and the V$_2$O$_3$@C host still maintains its basic nanorod-like morphology (Fig. 1e). The carbon nanorod skeleton and the anchored V$_2$O$_3$ can still be clearly seen from the TEM image of the SeS$_2$/V$_2$O$_3$@C (Fig. 1f), indicating their structural stability. The accordant color of the carbon nanorod region suggests the uniform dispersion of SeS$_2$ into the internal space of the V$_2$O$_3$@C (Fig. 1f and g). The interplanar of SeS$_2$ cannot be detected through high-resolution TEM, suggesting its amorphous nature. The STEM image and corresponding EDS mappings of the SeS$_2$/V$_2$O$_3$@C (Fig. 1h) further prove the uniform distribution of elemental C, V, O, S, and Se, which was also verified from the linear elemental distributions of the composite shown in Fig. S7.†

The phase compositions and microstructures of the samples were further investigated *via* XRD and Raman spectroscopy, respectively. Fig. 2a displays the XRD pattern of the V$_2$O$_3$@C, which shows a series of well-defined and strong characteristic peaks in addition to peaks ascribed to carbon nanorods. These peaks are well matched with that of the standard card (PDF# 71-0342), confirming the successful preparation of the target host materials. When the encapsulation of SeS$_2$ is completed, the XRD pattern of the SeS$_2$/V$_2$O$_3$@C exhibits far weaker peak signals of V$_2$O$_3$ and the absence of characteristic peaks ascribed to SeS$_2$. The absence of characteristic peaks ascribed to SeS$_2$ indicates the perfect infusion of SeS$_2$ within the internal nanopores of the host materials and its amorphous nature, as demonstrated in other similar literature.[22–24] This result was verified by the Raman spectra of the samples shown in Fig. S8,† which is obtained within a range from 100 to 2000 cm^{-1}, in which the Raman spectrum of SeS$_2$/V$_2$O$_3$@C does not feature the peaks of SeS$_2$ attributed to pure SeS$_2$. The amorphous SeS$_2$ can attain higher electrochemical reactivity to realize better electrochemical performance.[25–28] Besides this, the intensity ratio of the two constant dominant peaks located at 1359 and
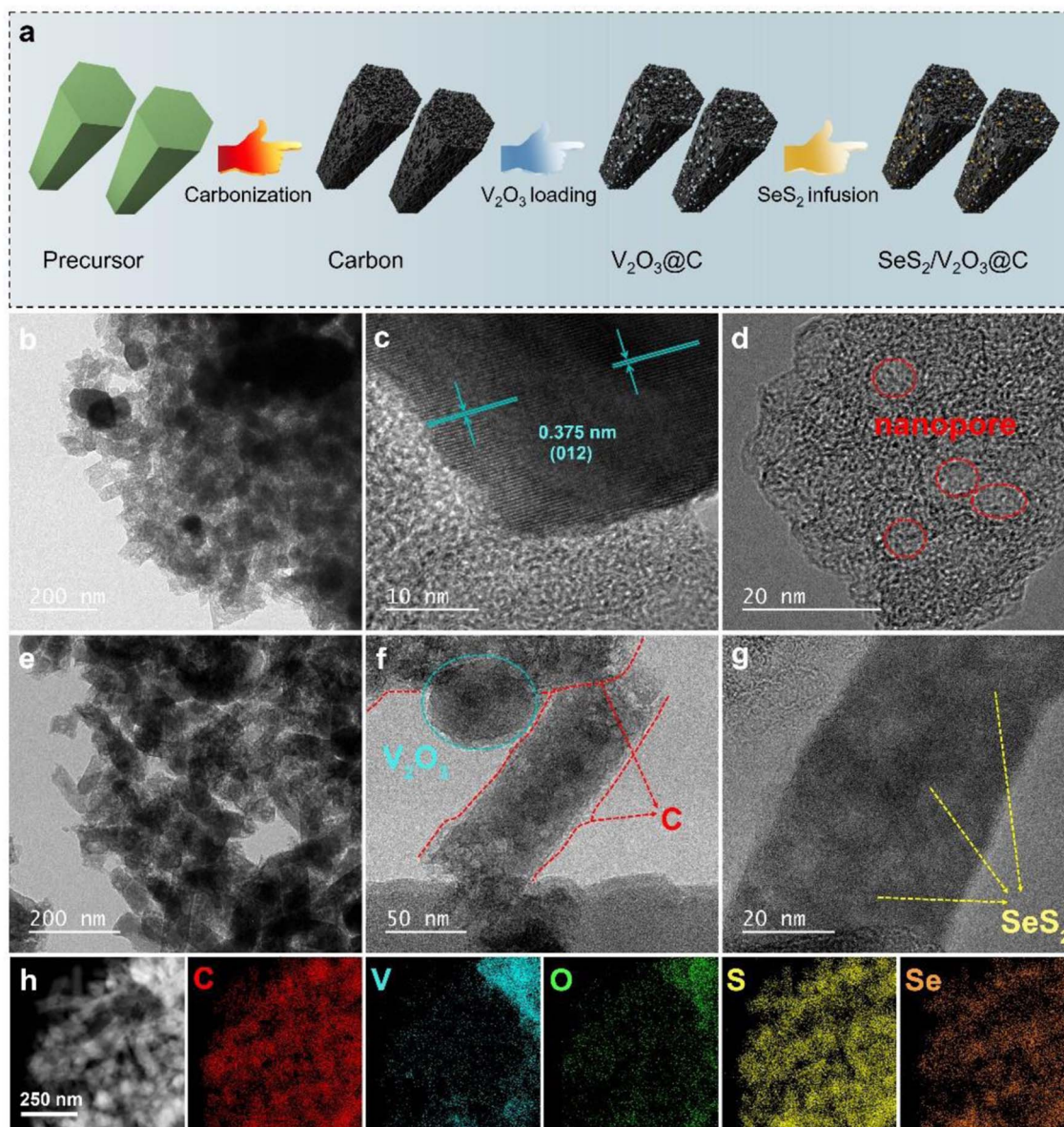
Fig. 1 (a) Schematic illustration of the synthetic procedure for the SeS$_2$/V$_2$O$_3$@C; (b–d) TEM and HRTEM images of the V$_2$O$_3$@C and (e–g) the SeS$_2$/V$_2$O$_3$@C; (h) STEM image and corresponding EDS mappings of the SeS$_2$/V$_2$O$_3$@C.

1594 cm^{-1} (D band and G band) indicates the graphitization degree of the carbon skeleton (*i.e.*, I_D/I_G).[29,30] The calculated I_D/I_G ratio value of 0.90 indicates the partially graphitized amorphous nature of the carbon skeleton, enabling fast electron transport in the electrochemical process.[29]

The porosity of the host materials usually plays a vital role in confining the dissolution of soluble species and alleviating the dramatic expansion of active materials. Here, the typical Brunauer–Emmett–Teller (BET) method was utilized to reveal the porous nature of all the samples, including their pore distribution, pore volume, and specific surface areas. As shown in Fig. 2b, the isotherm profile presents a dramatic rise in the low pressure region and an evident hysteresis in the high pressure region that suggest the existence of micropores and mesopores, respectively.[31,32] The carbon substrate has a high specific surface

area of 510 m^2 g^{-1} and a pore volume of 0.993 cm^3 g^{-1}. The specific size of the nanopores was further analyzed from the pore size distribution curve obtained *via* density functional theory (DFT), as shown in Fig. S9.† Micropores, mesopores, and macropores can all be clearly observed. After the encapsulation of SeS$_2$ into the carbon substrates, the plentiful nanopores disappear and the specific surface area is significantly decreased to 22 m^2 g^{-1} with a much smaller pore volume of 0.373 cm^3 g^{-1}. This indicates that the infused SeS$_2$ adequately occupies the internal nanocavities of the carbon substrate. The mass content of SeS$_2$ was determined as 60% of the whole SeS$_2$/V$_2$O$_3$@C nanocomposite, as shown in Fig. S10.† Notably, the temperature, at which the mass of the active materials was largely lost, was far higher than that of the preparation
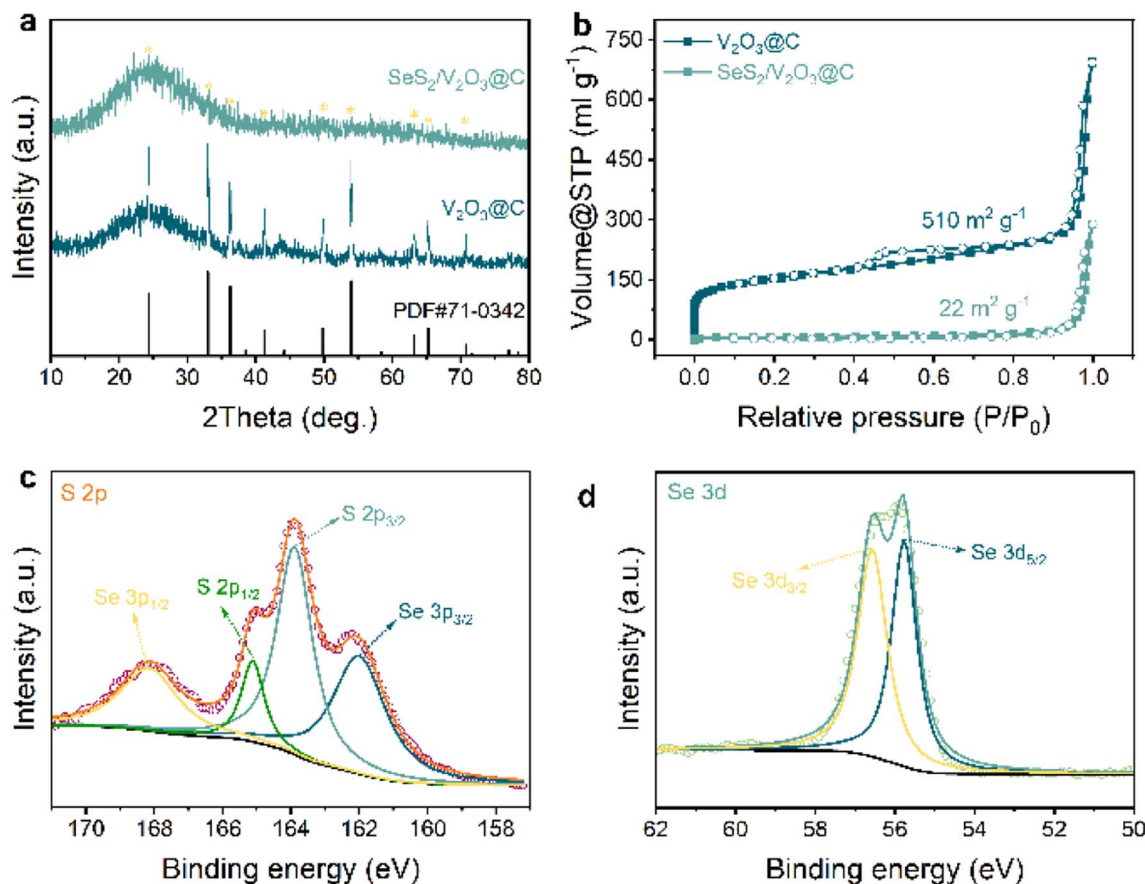
Fig. 2 (a) XRD patterns of $V_2O_3@C$ and $SeS_2/V_2O_3@C$; (b) nitrogen; (c) XPS spectra of S 2p; (d) XPS spectra of Se 3d.

temperature (160 °C), further demonstrating that the SeS_2 was completely confined within the carbon substrate.

X-Ray photoelectron spectroscopy (XPS) was conducted on the $SeS_2/V_2O_3@C$ sample to characterize the chemical states of the relevant elements. The survey spectrum of the sample in Fig. S11† shows the co-existence of elemental C, V, O, Se, and S, in good accordance with the aforementioned EDS mappings. Next, the high-resolution XPS spectra of the three key elements V, Se, and S were further analyzed. In the spectra of V (Fig. S12†), there are two dominant peaks located at 517 and 524.6 eV, respectively, which can be ascribed to the spin–orbit splitting of V 2p3/2 and V 2p1/2 and indicates a chemical state of +3.[33] Four clear peaks can be observed from the spectra of elemental S (Fig. 2c), which are positioned at 168.3, 165.1, 163.9, and 162.1 eV. The middle pair of peaks can be attributed to S–S bonds, while the two peaks at either side indicate the presence of Se–S bonds. Two peaks positioned at 55.8 and 56.6 eV reflect the elemental Se, as shown in Fig. 2d.

Owing to double design of host and guest, the as-obtained composite material is expected to realize excellent electrochemical performance. Accordingly, its sodium-ion storage capability was evaluated through assembling Na–SeS_2 batteries (Fig. 3). In order to investigate the redox mechanism of the $SeS_2/V_2O_3@C$ composite during the (de)sodiation process, cyclic voltammogram (CV) curves were recorded at a scan rate of

0.1 mV s^{-1} (Fig. 3a) and compared with previous literature. At the first cathodic scan, there is a sharp peak around 1.0 V but no obvious peaks above 1.0 V. This shows the activation process of SeS_2, where reduction reactions of SeS_2 into Na_2S/Na_2Se and electrolyte-associated decomposition reactions are involved.[19,34] At the corresponding anodic scan, Na_2S/Na_2Se is oxidized to S_8/Se_8 instead of pristine SeS_2 and the three oxidation peaks positioned at 1.8, 1.9, and 2.2 V reveal the stepwise conversion process from Na_2S/Na_2Se to S_8/Se_8. This result is highly consistent with other reports and implies the distinguished redox behavior of the SeS_2 cathode in different stages.[19,24] At the second cycle, the reduction peak at 2.2 V can be ascribed to conversion from S_8 to long-chain sodium polysulfides (Na_2S_x), and the two strong peaks at 1.6 and 1.0 V reflect reduction reactions from long-chain polysulfides/polyselenides to short-chain polysulfides/polyselenides and finally to Na_2S/Na_2Se, respectively.[35] The CV curves start to be stabilized from the third cycle, along with the appearance of three pairs of clear redox peaks, which suggest the reversible redox reactions of the cathode between S_8/Se_8 and Na_2S/Na_2Se and its electrochemical stability. As a whole, this mechanism is highly consistent with the pPAN/SeS_2 cathode reported by Lou et al.[19]

Fig. 3b displays the rate performance of the $SeS_2/V_2O_3@C$ and two control samples. The $SeS_2/V_2O_3@C$ shows high discharge capacities of 1319, 920, 850, 718, 693, and
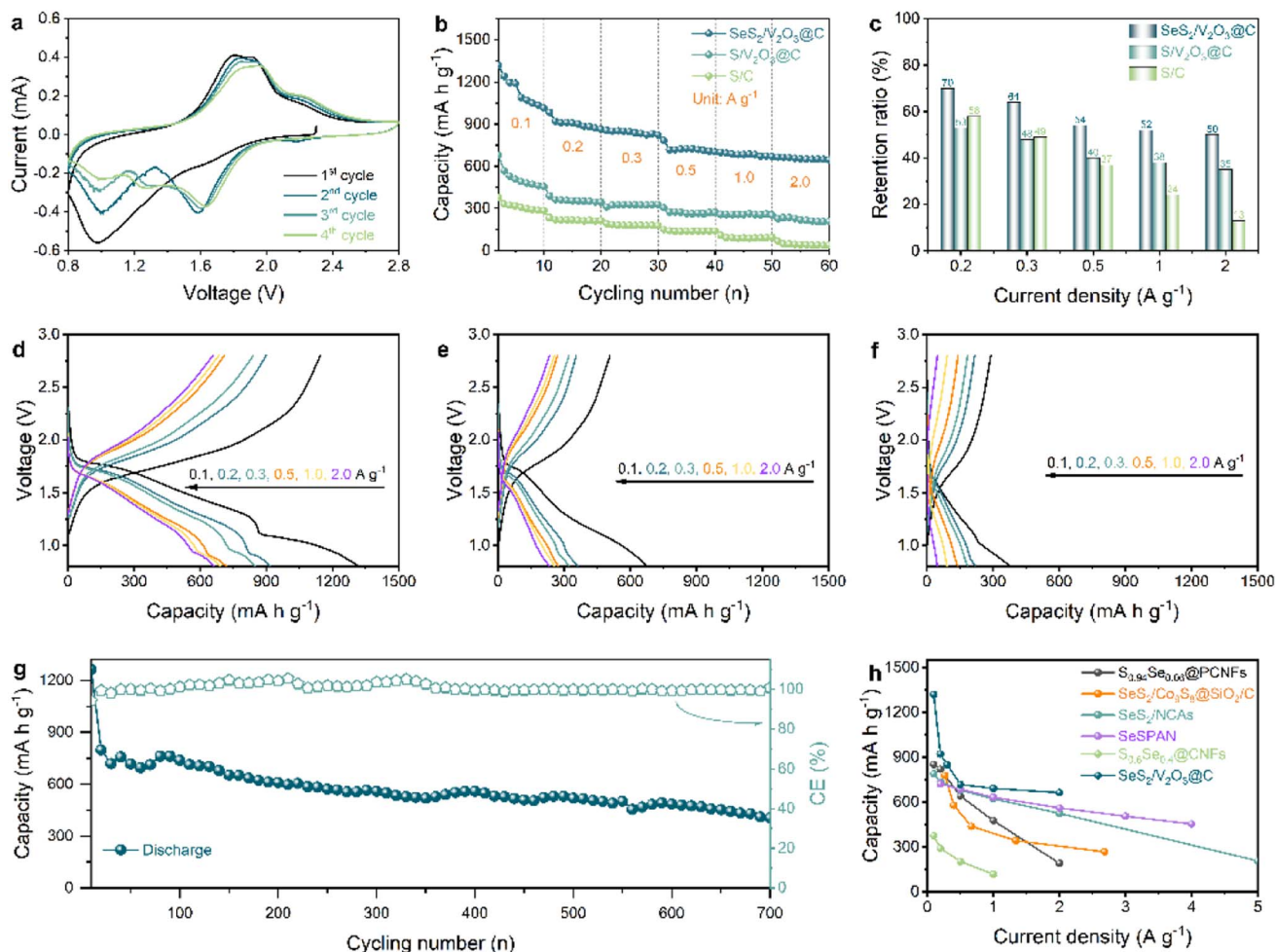
Fig. 3 (a) CV curves at 0.1 mV s^{-1}; (b) rate capabilities at different current densities; (c) capacity retention ratios based on 0.1 A g^{-1}; (d–f) discharge–charge profiles of SeS$_2$/V$_2$O$_3$@C, S/V$_2$O$_3$@C, and S/C at different current densities; (g) long-term cyclability of the SeS$_2$/V$_2$O$_3$@C composite at 1.0 A g^{-1}; (h) rate performance comparison between this work and other Se$_x$S$_y$ cathodes for Na-ion storage.

663 mA h g^{-1} at 0.1, 0.2, 0.3, 0.5, 1.0, and 2.0 A g^{-1}, respectively. In contrast, the S/V$_2$O$_3$@C and S/C composites show far lower discharge capacities of 362/221, 322/186, 274/142, 257/92, and 234/48 mA h g^{-1} at the corresponding rates. For acquiring deeper insight into the rate capability of these samples, the rate capacity retention ratio based on 0.1 A g^{-1} was calculated, as exhibited in Fig. 3c. The SeS$_2$/V$_2$O$_3$@C composite displayed

capacity retention ratios of 70, 64, 54, 52, and 50% at 0.2, 0.3, 0.5, 1.0, and 2.0 A g^{-1}, respectively. For the S/V$_2$O$_3$@C composite, capacity retention ratios of 53, 48, 40, 38, and 35% were obtained. As for the S/C composite, its capacity retention ratios were 58, 49, 37, 24, and 13%. It is worth mentioning that the SeS$_2$/V$_2$O$_3$@C and S/V$_2$O$_3$@C composites both show higher capacity retention ratios than that of the S/C composite at

Table 1 Comparison on the cycling performance of Se$_x$S$_y$ cathodes for Na-ion storage

| Material	Content	Voltage	Rate	Lifespan	Retention
This work	**60%**	**0.8–2.8 V**	**1 A g^{-1}**	**700**	**405.0 mA h g^{-1}**
SeS$_2$–C[36]	50.0%	0.8–2.8 V	0.05 A g^{-1}	30	228.0 mA h g^{-1}
S$_{0.6}$Se$_{0.4}$@CNFs[22]	60.0%	0.8–3.0 V	0.1 A g^{-1}	100	375.0 mA h g^{-1}
pPAN/SeS$_2$ (ref. 19)	69.0%	0.8–2.8 V	1 A g^{-1}	400	800 mA h g^{-1}
S$_{0.96}$Se$_{0.04}$@PCNFs[24]	72.0%	0.8–3.0 V	0.5 A g^{-1}	200	456.0 mA h g^{-1}
SeS$_2$/Co$_9$S$_8$@SiO$_2$/C[35]	40.0%	0.5–2.8 V	1C	300	191.0 mA h g^{-1}
CCN/SeS$_2$ (ref. 23)	70.0%	0.7–2.8 V	0.5 A g^{-1}	470	556.0 mA h g^{-1}
SeS$_2$@NCAs[37]	54.0%	1.0–3.0 V	0.5 A g^{-1}	1000	536.0 mA h g^{-1}
SeSPAN[38]	60.0%	0.8–2.8 V	0.5 A g^{-1}	150	632.0 mA h g^{-1}
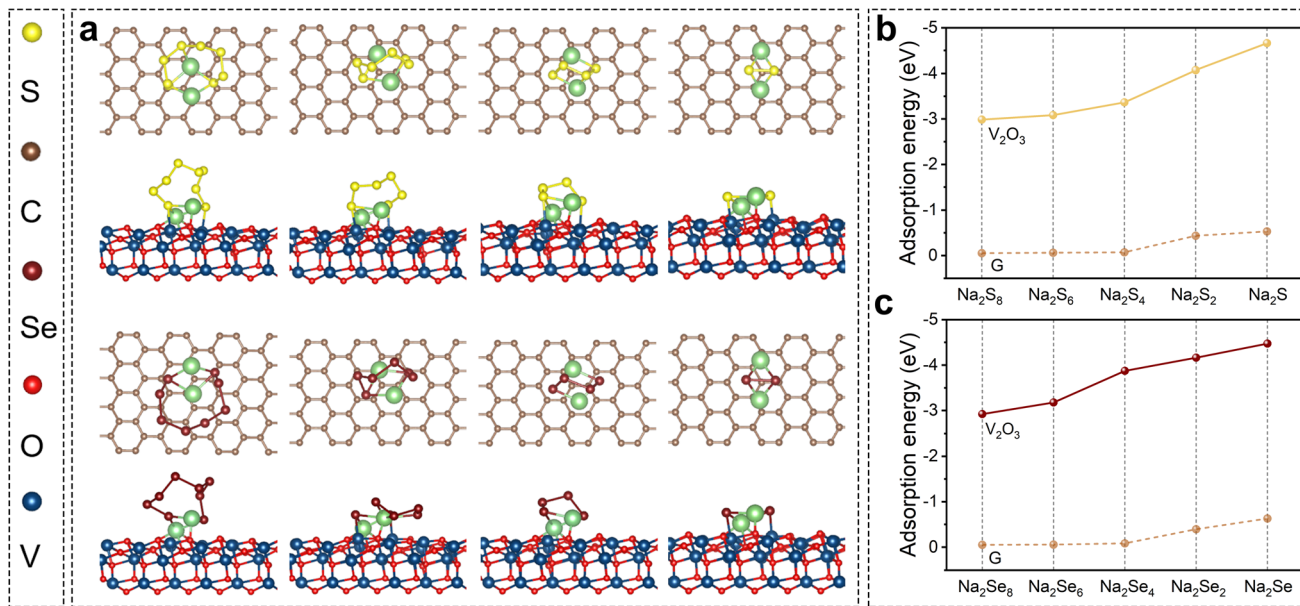
Fig. 4 (a) Molecular configurations between polysulfides/polyselenides and different substrates (graphene and V_2O_3); adsorption energy between graphene/V_2O_3 and (b) polysulfides or (c) polyselenides.

ultrahigh rates (1.0 and 2.0 A g^{-1}), suggesting that the incorporation of polar V_2O_3 plays a vital role in promoting rate capability. Next, we moved to the analysis of the discharge–charge profiles of these samples. The discharge–charge profiles of the SeS$_2$/V$_2$O$_3$@C in Fig. 3d show clear and overlapped voltage plateaus and low voltage polarization, which correspond very well to the aforementioned redox peaks, further indicating the highly reversible electrochemical reactions of the active materials. Conversely, the S/V$_2$O$_3$@C and S/C composites present shorter voltage plateaus, more inclined slopes, and far greater polarization (Fig. 3e and f). The better specific capacities, higher capacity retention ratios, and well-defined plateaus jointly demonstrate the enhanced rate performance of the SeS$_2$/V$_2$O$_3$@C composite in comparison with the S/V$_2$O$_3$@C and S/C composites. Besides this, the SeS$_2$/C composite shows negligible capacity improvement in comparison with the S/C composite, as shown in Fig. S13.† This proves that the performance improvement should be attributed to a synergistic effect between Se doping and the polar adsorbent instead of a single added component.

The long-term cyclability of the SeS$_2$/V$_2$O$_3$@C composite was also evaluated at a high current density of 1.0 A g^{-1}, as illustrated in Fig. 3g. For full activation of the active materials, the SeS$_2$/V$_2$O$_3$@C composite cathode was pre-cycled for 20 cycles at 0.1 A g^{-1}. Afterwards, a discharge specific capacity of 798 mA h g^{-1} was observed and a high discharge specific capacity of 405 mA h g^{-1} was still retained after 700 cycles. In addition to that, an ultrahigh coulombic efficiency of close to 100% is observed, suggesting high energy conversion efficiency. Fig. S14† shows the cycling performance of the V$_2$O$_3$@C composite under the same test conditions, which can be ignored due to the low contribution and suggests that the capacity of the whole cathode is from the reversible conversions

of the active materials. The long cyclability of the electrode is superior to the reports of most studies regarding Na–Se$_x$S$_y$ batteries through comprehensively considering multiple factors such as current density, lifespan, and capacity retention.[19,22–24,35–38] Table 1 summarizes the long-term cycling stability of currently reported Se$_x$S$_y$ cathodes for Na-based batteries. Furthermore, the rate capabilities are compared with those of studies on Na–Se$_x$S$_y$ batteries. It can be clearly seen from Fig. 3h that the rate capabilities of the as-designed SeS$_2$/V$_2$O$_3$@C composite are obviously higher than most of the values reported in the literature.[22,24,35,37,38] To explore the influence of active material loading content on the performance of the cathodes, the loading content of SeS$_2$ in the composite was elevated to 70%. As shown in Fig. S15,† the SeS$_2$ cathode with a higher content shows the worst cycling performance. This enlightens that more work needs to be done to realize high-loading electrodes with excellent performance in the future.

The aforementioned excellent electrochemical performance should be attributed to the double design of the SeS$_2$/V$_2$O$_3$@C composite in terms of chemical compositions of both the host and guest materials, which can potentially help to stabilize the cathode and improve the reaction kinetics. The immobilization effect of V$_2$O$_3$ for soluble intermediates was explored via theoretical and experimental evidence. DFT calculations were conducted on graphene and V$_2$O$_3$ to gain insight into molecular configurations and adsorption energy, as displayed in Fig. 4 and S16.† Various polysulfides/polyselenides cannot chemically bond with pure graphene. This suggests that pure carbon substrate is unable to interact with these soluble polysulfides/polyselenides via strong chemical bonds instead of weak van der Waals forces. In contrast, polysulfides interact with the surface atoms of V$_2$O$_3$ via Na–O and V–S bonds. Likewise, a series of polyselenides tend to couple with V$_2$O$_3$ to generate
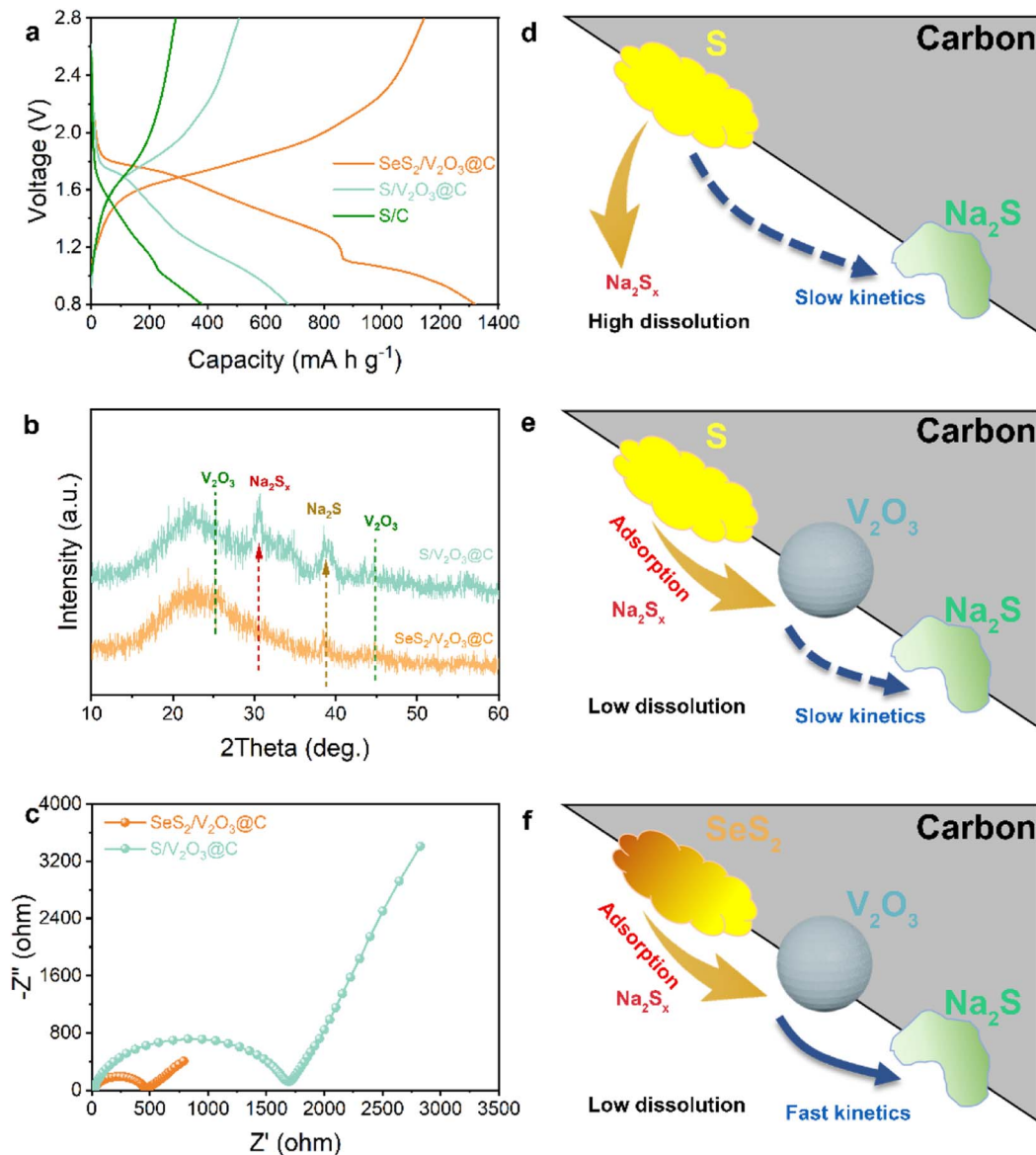
Fig. 5 (a) Discharge–charge profiles of three samples at the same rate; (b) XRD patterns of the SeS$_2$/V$_2$O$_3$@C and S/V$_2$O$_3$@C composite after cycling; (c) EIS spectra of the SeS$_2$/V$_2$O$_3$@C and S/V$_2$O$_3$@C; (d–f) schematic illustrations of the electrochemical behavior of different samples.

Na–O and V–Se bonds. The chemical affinity of V$_2$O$_3$ for polysulfides/polyselenides can be quantificationally determined from their adsorption energies. The adsorption energies of polysulfides/polyselenides with different substrates are shown in Fig. 4b and c. The adsorption energies of Na$_2$S$_n$ (n = 8, 6, 4, 2, and 1) on graphene were −0.06, −0.05, −0.07, −0.44, and −0.53 eV, respectively, while the adsorption energies on the V$_2$O$_3$ surface were −2.99, −3.09, −3.37, −4.66, and −4.07 eV, respectively. The adsorption energies of Na$_2$Se$_n$ (n = 8, 6, 4, 2, and 1) on the graphene were −0.08, −0.06, −0.05, −0.39, and −0.63 eV, respectively, while the adsorption energies on the V$_2$O$_3$ surface were −2.93, −4.47, −3.18, −4.16, and −3.87 eV, respectively. This fully demonstrates the great chemical affinity of V$_2$O$_3$ for various polysulfides/polyselenides. Besides this, it is also worth mentioning that with an increase in the chain length

of polysulfides and polyselenides, the adsorption energy is relatively lowered (weakened chemical bonds), suggesting that polysulfides/polyselenides easily dissociate into shorter-chain sulfides on the surfaces of V$_2$O$_3$.

These results are further supported by optical observations, UV-vis spectroscopy of the polysulfide solutions, and XPS spectra of the sample before and after discharging. As shown in Fig. S17a,† Na$_2$S$_6$ solution was prepared as a representative of polysulfides/polyselenides to be soaked with different samples and further observe its color change after standing for 12 h. The solution soaked with the pure carbon substrate remained the same yellow color as the blank solution, while the solution soaked with V$_2$O$_3$@C became colorless and transparent. At the same time, the absorbance intensity of the solution soaked with the V$_2$O$_3$@C was significantly reduced (Fig. S17b†), suggesting

complete adsorption of the polysulfide molecules. This contrast effectively proves the strong chemical affinity of the V_2O_3 for polysulfides. Moreover, the XPS spectra of elemental V from the $SeS_2/V_2O_3@C$ composite cathode undergoes an evident shift after discharging to 2.0 V (Fig. S17c†), indicating chemical bonding between S/Se-based products and $V_2O_3@C$ in the electrochemical process.

Apart from efficient immobilization of the active materials, the fast conversion of the cathodes with high kinetics can also contribute to improving the electrochemical performance to a large extent. The above discussion highlighted the adsorption effect of V_2O_3 for soluble intermediates, so the improvement effect of the Se doping on conversion kinetics will be discussed next. As shown in Fig. 5a, $SeS_2/V_2O_3@C$ exhibits much lower voltage polarization than that of the $S/V_2O_3@C$, suggesting that the Se dopant promotes the kinetical conversion of S guests. Fig. 5b displays the XRD patterns of the cycled $SeS_2/V_2O_3@C$ and $S/V_2O_3@C$ electrodes. The latter suffers from more obvious electrochemical deposition of Na_2S_x and Na_2S in comparison to the former. This indicates that the Se doping is able to facilitate the reversible conversion of the active S molecules to lower the accumulation of inactive species and deliver higher capacity. The $SeS_2/V_2O_3@C$ shows a much lower electron transfer impedance than that of $S/V_2O_3@C$, which is conducive to promoting a faster electrochemical reaction rate (Fig. 5c), suggesting the improved electronic conductivity of the whole electrode is induced by the Se dopant. The CV curves at various scan rates were recorded to analyze the Na-ion diffusion behavior (Fig. S17†). It can be observed that despite increased current density, the CV curve still presents clear redox peaks and a strong current response, which are indicators of the electrochemical stability of electrodes. Furthermore, the peaks can be linearly fitted to attain the b value and determine the electrochemical behavior of Na ions based on their scan rates and current response. As is known, Na-ion transfer is controlled by diffusion if the b value is close to 0.5, while it exhibits capacitance with faster kinetics if the b value is close to 1.0.[39,40] As shown in Fig. S19,† the reduction and oxidation process both show b values of 0.79 and 0.80, respectively, which suggest the redox reactions of the $SeS_2/V_2O_3@C$ composite cathode exhibit fast conversion kinetics.

Specially, post-analyses are carried out through disassembling the batteries after cycling to further characterize the stability of the as-designed cathode. Fig. S20† shows the separators from batteries assembled with different cathodes. The separator from that with the S/C cathode is obviously yellow, suggesting the dissolution and shuttling of the S species. The separator from that with $S/V_2O_3@C$ is slightly yellow, suggesting that the V_2O_3 effectively helps to inhibit the shuttle effect of polysulfides to a large extent. In contrast, the separator from that with $SeS_2/V_2O_3@C$ remains white, suggesting the completely controlled shuttle effect via the joint action of V_2O_3 implantation and Se doping. Besides this, the microscopic morphology of the cycled electrode was observed via the TEM (Fig. S21†) imaging of multiple regions, where the materials still maintains its nanorod shape. This confirms the structural stability of the substrate materials, which can assist in

alleviating the mechanical stress from the volume change of the active materials and consequently induces a prolonged cycling lifespan. The STEM with corresponding EDS mappings in Fig. S22† reveals the uniform distribution of all elements after the cycling process. The observable elemental F and Cl are products of the decomposition reactions of electrolyte to construct the cathode interface layer, as the sample is fully cleaned before testing.

As a whole, the excellent electrochemical properties of the as-designed $SeS_2/V_2O_3@C$ composite result from the synergistic effect of polar V_2O_3 and doped Se, in which the V_2O_3 plays a significant role in adsorbing soluble polysulfides/polyselenides to stabilize the whole cathode without loss of the active materials and the Se dopant is responsible for improving the electronic conductivity of the S molecules and accelerating the conversion kinetics. The carbon substrate offers a conductive network for fast electron transport and accommodates the volume effect of the active materials during the electrochemical process. The synergistic mechanism is schematically illustrated in Fig. 5d–f.

Conclusion

In summary, we presented a double design strategy of a carbon host and S guest to fabricate a $SeS_2/V_2O_3@C$ composite for preparing S cathodes with enhanced electrochemical properties. Theoretical and experimental evidence has shown that the polar V_2O_3 nanoparticles implanted into carbon nanorods are able to chemically adsorb the soluble sodium polysulfides/polyselenides via strong chemical affinity and the Se dopant regulates the electronic structure of the S molecules, improving their electronic conductivity and promoting the redox conversion of S species. The synergistic effect between Se doping and polar V_2O_3 inhibits the shuttle effect and induces better reaction kinetics, eventually leading to outstanding electrochemical performance. The work sheds light on the significance of the co-design of host and guest as well as provides a new pathway to improve the overall properties of Na–S batteries.

Experimental section

Preparation of the precursor

First, 1.20 g of 2,5-dihydroxyterephtalic acid and 2.016 g of zinc acetate dihydrate were separately dissolved in mixed solutions of deionized water and dimethylformamide. Afterwards, these two solutions were mixed and stirred for 30 min. Then, the uniform solution obtained was transferred into a Teflon-lined autoclave and heated for 24 h at 100 °C. After that, the resulting solid precipitate was centrifuged, washed with ethanol, and dried overnight at 80 °C to produce the precursor.

Preparation of carbon and $V_2O_3@C$

The precursor was placed into a tube furnace and annealed for about 4.5 h at 900 °C under an Ar atmosphere. After cooling, the black powder was carbon nanorods. 500 mg of the carbon nanorods and 400 mg of vanadium chloride were dispersed in
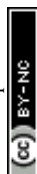
20 mL of ethanol *via* stirring for 12 h. After this time, the solution was dried for 8 h at 80 °C. The as-obtained black powder was further annealed for 5 h at 900 °C under an Ar atmosphere at a heating rate of 5 °C min^{-1} to produce V_2O_3@C.

Preparation of SeS₂/V₂O₃@C

SeS_2 powder and V_2O_3@C powder were mixed, ground, and heated for 12 h at 160 °C to produce the SeS_2/V_2O_3@C composite. The control sample S/V_2O_3@C was fabricated using the same method, except that a temperature of 155 °C was used.

Materials characterization

The morphologies of the samples were observed *via* FESEM (ZEISS, GeminiSEM 300) and TEM (Tecnai G2 F20 S-TWIN). The elemental distributions were acquired by energy-dispersive X-ray spectroscopy (EDS). The crystal structures were analyzed using an X-ray diffractometer (XRD) equipped with a Cu Kα radiation source. X-ray photoelectron spectroscopy (XPS, Thermo Scientific ESCALAB 250Xi) was used to characterize the chemical states of the elements. Raman spectra were examined using an InviaRefl (Renishaw, UK) equipped with a 532 nm laser. The porosity was tested using the Brunauer–Emmett–Teller method (BSD PS2, China). Thermal analysis was evaluated by thermogravimetric analysis (TG 209, Germany).

Electrochemical measurements

The target materials, Ketjen black, and PVDF were ground in a mass ratio of 8 : 1 : 1 to form a black slurry. The resulting slurry was then coated on carbon-coated Al foil and further dried at 80 °C. The areal mass loading content was 1.2–1.5 mg cm^{-2}. The amount of electrolyte in every coin cell was 50 μL. The cathode slice, Na foil, and glass fiber were assembled into 2032-type coin cells in an argon-filled glove box with an oxygen/water content of <0.01 ppm. The electrolyte was 1 M $NaClO_4$ salt dissolved in a EC-PC (1 : 1) mixed solvent with 5 wt% FEC additive. An electrochemical workstation (Chenhua Instrument, CHI 660E) was harnessed to measure CV curves over a voltage window of 0.8–2.8 V and EIS spectra were recorded over a frequency range from 0.01 Hz to 100 kHz. The galvanostatic discharge–charge properties were measured on a LAND instrument testing system.

Calculation details

First-principle calculations were implemented in the VASP program based on density functional theory. The generalized gradient approximation of Perdew–Burke–Ernzerhof was employed for investigating the electronic exchange and correlation. The plane wave pseudopotential with a kinetic cutoff energy of 450 eV within the projector augmented wave (PAW) method was utilized. van der Waals dispersion-corrected DFT (DFT-D3) was also performed. The self-consistent total energy convergence criteria were less than 10^{-4} eV. The geometry optimization was finalized once the forces on all atoms were smaller than 0.02 eV Å^{-1}. The K-point was produced using a $3 \times 3 \times 1$ grid employing the Monkhorst–Pack method. The cell parameters ($a \times b \times c$) were $4 \times 4 \times 1$ for graphene and $2 \times 1 \times 1$ for V_2O_3 (012), respectively. All surface models were constructed under vacuum conditions of ∼15 Å along the c-axis. The absorbed energies between slab materials (graphene and V_2O_3) and different Na_2S_n/Na_2Se_n molecules were calculated according to the equation: $E_{ad} = E_{(slab+molecules)} - E_{slab} - E_{molecules}$.

Author contributions

X. L. H. conceived the project, carried out the experiments, and wrote the manuscript. H. Z., C. L., Y. L., and S. Z. performed the materials characterization. Y. W., W. Z., and H. K. L. read and edited the manuscript. S. X. D. and Z. W. had advisory roles in the project and completing the manuscript.

Conflicts of interest

The authors declare no competing financial interest.

Acknowledgements

References

1 Y. Qi, Q.-J. Li, Y. Wu, S.-j. Bao, C. Li, Y. Chen, G. Wang and M. Xu, *Nat. Commun.*, 2021, **12**, 6347.

2 X. L. Huang, Y.-X. Wang, S.-L. Chou, S. X. Dou and Z. M. Wang, *Energy Environ. Sci.*, 2021, **14**, 3757–3795.

3 Y. Wang, D. Zhou, V. Palomares, D. Shanmukaraj, B. Sun, X. Tang, C. Wang, M. Armand, T. Rojo and G. Wang, *Energy Environ. Sci.*, 2020, **13**, 3848–3879.

4 X. L. Huang, S. X. Dou and Z. M. Wang, *Mater. Horiz.*, 2021, **8**, 2870–2885.

5 X. L. Huang, X. Zhang, L. Zhou, Z. Guo, H. K. Liu, S. X. Dou and Z. Wang, *Adv. Sci.*, 2022, 2206558.

6 X. Xu, D. Zhou, X. Qin, K. Lin, F. Kang, B. Li, D. Shanmukaraj, T. Rojo, M. Armand and G. Wang, *Nat. Commun.*, 2018, **9**, 3870.

7 H. Liu, W. Pei, W.-H. Lai, Z. Yan, H. Yang, Y. Lei, Y.-X. Wang, Q. Gu, S. Zhou, S. Chou, H. K. Liu and S. X. Dou, *ACS Nano*, 2020, **14**, 7259–7268.

8 X. Ye, J. Ruan, Y. Pang, J. Yang, Y. Liu, Y. Huang and S. Zheng, *ACS Nano*, 2021, **15**, 5639–5648.

9 H. Liu, W.-H. Lai, Y. Liang, X. Liang, Z.-C. Yan, H.-L. Yang, Y.-J. Lei, P. Wei, S. Zhou, Q.-F. Gu, S.-L. Chou, H. K. Liu, S. X. Dou and Y.-X. Wang, *J. Mater. Chem. A*, 2021, **9**, 566–574.

10 X. L. Huang, S. X. Dou and Z. M. Wang, *Energy Storage Mater.*, 2022, **45**, 265–280.

11 Z. Yan, J. Xiao, W. Lai, L. Wang, F. Gebert, Y. Wang, Q. Gu, H. Liu, S.-L. Chou, H. Liu and S.-X. Dou, *Nat. Commun.*, 2019, **10**, 4793.

12 C. Wu, Y. Lei, L. Simonelli, D. Tonti, A. Black, X. Lu, W.-H. Lai, X. Cai, Y.-X. Wang, Q. Gu, S.-L. Chou, H.-K. Liu, G. Wang and S.-X. Dou, *Adv. Mater.*, 2022, **34**, 2108363.

13 Y.-X. Wang, J. Yang, W. Lai, S.-L. Chou, Q.-F. Gu, H. K. Liu, D. Zhao and S. X. Dou, *J. Am. Chem. Soc.*, 2016, **138**, 16576–16579.

14 A. Y. S. Eng, Y. Wang, D.-T. Nguyen, S. Y. Tee, C. Y. J. Lim, X. Y. Tan, M.-F. Ng, J. Xu and Z. W. Seh, *Nano Lett.*, 2021, **21**, 5401–5408.

15 F. Xiao, X. Yang, H. Wang, J. Xu, Y. Liu, D. Y. W. Yu and A. L. Rogach, *Adv. Energy Mater.*, 2020, **10**, 2000931.

16 J. Zhou, Y. Yang, Y. Zhang, S. Duan, X. Zhou, W. Sun and S. Xu, *Angew. Chem., Int. Ed.*, 2021, **60**, 10129–10136.

17 A. Kumar, A. Ghosh, A. Roy, M. R. Panda, M. Forsyth, D. R. MacFarlane and S. Mitra, *Energy Storage Mater.*, 2019, **20**, 196–202.

18 S. Li, Z. Zeng, J. Yang, Z. Han, W. Hu, L. Wang, J. Ma, B. Shan and J. Xie, *ACS Appl. Energy Mater.*, 2019, **2**, 2956–2964.

19 Z. Li, J. Zhang, Y. Lu and X. W. Lou, *Sci. Adv.*, 2018, **4**, eaat1687.

20 L. Wang, X. Chen, S. Li, J. Yang, Y. Sun, L. Peng, B. Shan and J. Xie, *J. Mater. Chem. A*, 2019, **7**, 12732–12739.

21 Y. Sun, J. Liao, J. Sun, L. Duan, Y. Du, J. Bao and X. Zhou, *ACS Appl. Energy Mater.*, 2022, **5**, 13023–13030.

22 Y. Yao, L. Zeng, S. Hu, Y. Jiang, B. Yuan and Y. Yu, *Small*, 2017, **13**, 1603513.

23 J. Ma, L. Gao, S. Li, Z. Zeng, L. Zhang and J. Xie, *Batteries Supercaps*, 2020, **3**, 165–173.

24 L. Zeng, Y. Yao, J. Shi, Y. Jiang, W. Li, L. Gu and Y. Yu, *Energy Storage Mater.*, 2016, **5**, 50–57.

25 C. Feng, X. L. Huang, Y. Li, Y. Wang, C. Li, W. Qiu, S. Zhang, H. Liu, Y. Zhang, H. K. Liu, S. X. Dou and Z. Wang, *Chem. Eng. J.*, 2022, **442**, 136189.

26 C. Liu, X. Huang, J. Wang, H. Song, Y. Yang, Y. Liu, J. Li, L. Wang and C. Yu, *Adv. Funct. Mater.*, 2018, **28**, 1705253.

27 H. Zhang, L. Zhou, X. Huang, H. Song and C. Yu, *Nano Res.*, 2016, **9**, 3725–3734.

28 C. Shen, T. Wang, X. Xu and X. Tian, *Electrochim. Acta*, 2020, **349**, 136331.

29 X. L. Huang, X. Zhang, M. Yi, Y. Wang, S. Zhang, S. Chong, H. K. Liu, S. X. Dou and Z. Wang, *Chem. Sci.*, 2022, **13**, 11585–11593.

30 X. L. Huang, P. Xiang, H. Liu, C. Feng, S. Zhang, Z. Tian, H. K. Liu, S. X. Dou and Z. Wang, *Inorg. Chem. Front.*, 2022, **9**, 5486–5494.

31 X. Huang, J. Deng, Y. Qi, D. Liu, Y. Wu, W. Gao, W. Zhong, F. Zhang, S. Bao and M. Xu, *Inorg. Chem. Front.*, 2020, **7**, 1182–1189.

32 L. Zhang, B. Zhang, Y. Dou, Y. Wang, M. Al-Mamun, X. Hu and H. Liu, *ACS Appl. Mater. Interfaces*, 2018, **10**, 20422–20428.

33 X. Liu, Z. Wang, Y. Niu, C. Liu, H. Chen, X. Ren, Z. Liu, W.-M. Lau and D. Zhou, *ACS Appl. Energy Mater.*, 2022, **5**, 3525–3535.

34 Y. Lei, C. Wu, X. Lu, W. Hua, S. Li, Y. Liang, H. Liu, W.-H. Lai, Q. Gu, X. Cai, N. Wang, Y.-X. Wang, S.-L. Chou, H.-K. Liu, G. Wang and S.-X. Dou, *Angew. Chem., Int. Ed.*, 2022, **61**, e202200384.

35 T. Yang, Y. Qi, W. Zhong, M. Tao, B. Guo, Y. Wu, S.-J. Bao and M. Xu, *Adv. Funct. Mater.*, 2021, **31**, 2001952.

36 A. Abouimrane, D. Dambournet, K. W. Chapman, P. J. Chupas, W. Weng and K. Amine, *J. Am. Chem. Soc.*, 2012, **134**, 4505–4508.

37 Y. Deng, L. Gong, H. Ahmed, Y. Pan, X. Cheng, S. Zhu and H. Zhang, *Nano Res.*, 2020, **13**, 967–974.

38 V. H. Pham, J. A. Boscoboinik, D. J. Stacchiola, E. C. Self, P. Manikandan, S. Nagarajan, Y. Wang, V. G. Pol, J. Nanda, E. Paek and D. Mitlin, *Energy Storage Mater.*, 2019, **20**, 71–79.

39 X. Zhou, Z. Yu, Y. Yao, Y. Jiang, X. Rui, J. Liu and Y. Yu, *Adv. Mater.*, 2022, **34**, 2200479.

40 H. Hao, Y. Wang, N. Katyal, G. Yang, H. Dong, P. Liu, S. Hwang, J. Mantha, G. Henkelman, Y. Xu, J. A. Boscoboinik, J. Nanda and D. Mitlin, *Adv. Mater.*, 2022, **34**, 2106572.